Wave drag reduction due to a self aligning aerodisk

Christian Schnepf, Oliver Wysocki and Erich Schülein
German Aerospace Center (DLR)
Bunsenstr. 10, 37073 Göttingen, Germany

Abstract

The effect of a self-aligning aerodisk on the wave drag of a blunt slender body in a pitching maneuver has been numerically investigated. With a coupling of the flow solver and a 6DOF-tool the self-alignement was realized. The slender body is pitching with high repetition rate between $\alpha = 0°$ and $\alpha = 20°$ at $M = 1.41$. In comparison to the reference body without a self-aligning aerodisk a distinct drag reduction is achieved. A comparison with existing experimental data shows qualitatively a very good agreement considering the shock and separation structure and the kinematics of the aerodisk.

1. Introduction

One of the most important aerodynamic design goals was and is the reduction of aerodynamic drag. No matter whether a flight object is flying with subsonic or supersonic speed, the drag is limiting its speed and range. At supersonic speed the wave drag or pressure drag plays the most important role. As a result a round and rather blunt nose favoured in subsonic and transonic flight has a large drawback in supersonic flight, due to the occurring bow shock, see Fig. 1a. Its strength and the accompanied total pressure loss is increased with increasing Mach number. Considering only aerodynamics, sharp and pointed nose with a high finess ratio is most beneficial at this speed range [1]. In this case the bow shock is transformed to a weaker conical or oblique shock. But the available space in a cone or a tangent ogive nose is limited and also the length of a missile is increased using a high-finess-ratio nose. Therefore it is not practicable for the integration of avionics or a seeker. From this point of view a blunt nose is preferred.

A well known concept of reducing the impact of the bow shock, while keeping a blunt nose is the aerospike concept [2]. A thin rod mounted on the tip of a blunt body is the simplest design of an aerospike, see Fig.1b. The beneficial effect on the drag is investigated since decades [3] and already applied in missiles like Trident C-4 und C-5. Slight variations of the initial design include cones, spheres or disks that are additionally mounted on the tip of the rod. Nowadays also several alternative concepts to the aerospike exists. The concepts range from energizing the air in front of the blunt body due to laser heating (e.g. [4, 5]), DC-Arc discharge (e.g. [6]) or microwaves (e.g. [7]) to inject counterflow jets existing of air (e.g. [8, 9]) or plasma (e.g. [10, 11]). Most of the concepts induce a similar flow pattern

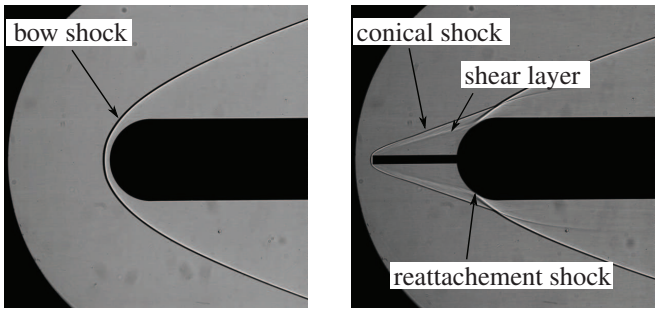

(a) Without spike (b) With spike

Figure 1: Shadowgraphy of a Bow Shock and a spike induced separation on a hemispherical model at $M = 5$, $\alpha = 0°$[14].

in front of the blunt body like the aerospike. Because of the strong interest in aerospikes and related concepts several reviews were published in the past e.g. [2] and recently [12].

Considering the aerospike in the ideal case the boundary layer on the rod separates along the whole rod surface due to the pressure rise over the conical shock [13], see Fig. 1b. The separated boundary layer forms a shear layer that reattaches on the blunt nose. Due to the shear layer the outer supersonic flow is deflected and a weaker conical shock is formed instead of the inital bow shock. Just in front of the spike tip a detached bow shock exists. The conical shock units further downstream with the reattachment shock. Inside the shear surface a recirculation zone exists that shows significantly lower pressure levels compared with the blunt body without an aerospike. With this simple method a drag reduction of more than 50 percent can be achieved, but only if the spike is aligned with the oncoming flow [14]. This is also valid for the alternative concepts. The effectivity of a spike decreases with increasing angle of attack α. In the cited experimental investigation at $\alpha > 15°$ -$\alpha = 20°$, dependent on M and the spike geometry, no drag reduction was observable anymore. In some cases the drag was even increased with a spike. At a certain angle of attack a favoured shock system like in Fig. 1a is not achievable anymore (Fig. 2a).

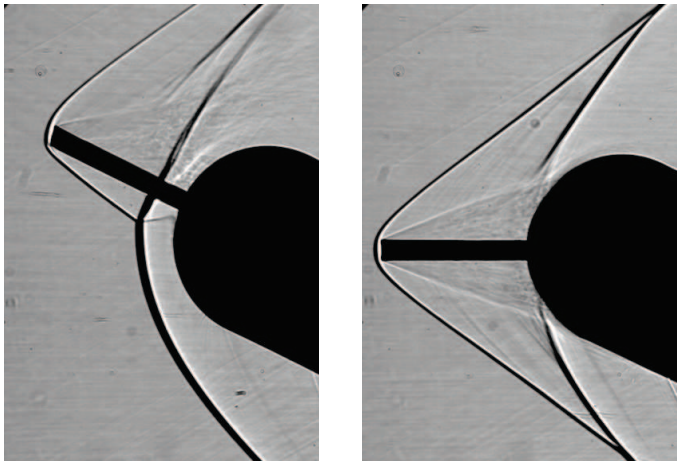

(a) Not aligned (b) Aligned

Figure 2: Shadowgraphy of a fixed and an aligned spike at M = 2, $\alpha = 20°$ [14].

High maneuverability is a major requirement for some flight missions of a modern missile today. Hence an extension of the range of α where a spike significantly reduces the drag is desirable. One method is the "Self-aligning aerospike" concept [15]. Here a movable spike ideally points always in the direction of the oncoming flow even though the main body shows an angle of attack. The favourable shock system in front of the nose can be sustained (Fig. 2b) and so does the reduction of the pressure drag at the nose. The effect of a self-aligned aerospike has already been demonstrated in the "Proof-of-Concept experiment" [14] as well as in the experimental investigations [16] on a generic missile pitching at high frequencies. The spike respectively a disk was mounted on a frame, rotatable about the nose (Fig 3). On the other end of the frame small vanes were attached. The aerodynamic forces acting on the vanes induced a pitching moment about the hinge and aligned the disk with the oncoming flow.

The present paper is a numerical realization of this version of a self-aligning-aerodisk. Like in the experiments the aerodisk should be aligned with the oncoming flow due to aerodynamic forces therefore a six degree of freedom flight mechanic tool (6DoF) has to be coupled with a flow solver. To realize the movement of the aerodisk relatively to the slender body the chimera technique is used. Because only a simplified body is simulated only a qualitative comparison is made with the corresponding experiments. For reference purposes the results with aerodisk are compared with the results of a pitching slender body without an aerodisk.

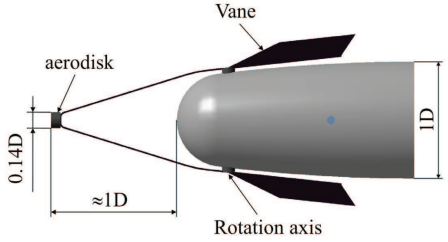

Figure 3: Model nose with self aligning spike.

2. Test Model Geometry and Computational Grid

The self-aligning disk-wing concept is numerically investigated at the forebody of the generic missile geometry that was used in the experiments [16]. The CFD-model geometry consists of a cylinder with a blunt ogival nose (SB), with a total length of $l_M = 269\ mm$ and a diameter of $D = 36\ mm$. The finess ratio of the nose (semi-sphere+ogive) is 1.92. In Fig. 3 the nose with the aerodisk device (AD) is shown. The aerodisk device consists of a disk with a diameter of $d = 5$ mm. The disk is placed $l = 39.3$ mm in front of the blunt nose. It is mounted on a frame. This frame shows on his right end aerodynamic lifting surfaces (Fig. 3). A joining rod and a hinge for bearing is not part of the geometry used in the CFD. Apart from this the simulated geometry is consistent with the corresponding parts of the geometry of the experimental investigation [16].

The pitching motion of the AD about the nose of the SB is realized with the cutting hole chimera technique. Two grids are required for this approach, one for the SB and one for the AD (Fig. 4). These grids are superimposed to obtain the geomtery in Fig. 4c and the actual computational grid. The AD grid can pitch within the SB grid about the nose. In Fig. 4a the grey frame is the outer boundary of the AD grid and in the solver defined as chimera boundary condition. The common farfield boundary is defined in the SB grid. The chimera technique in general makes it possible to solve the (U)RANS equation on overlapping grids. At the region where the grids are overlapping the flow properties are interpolated from one grid to the other. A more detailed explanation can be found in [17]. The difficulty in the present study considering the chimera technique is the large variation of possible interspace between viscous walls of the two grids. For example at $\alpha = 0°$ the vanes and the frame of AD are very close to the cylinder surface of the SB. At high α the interspace between both components is quite large. For the chimera technique the best quality in interpolation is achieved if the grids have the same cell size where they overlap respectively a chimera boundary is. Therefore the bottom of the AD grid consists of two layers, the layer closer to the AD geometry shows smaller cell sizes (L1), the layer right at the bottom larger cell sizes (L2), see Fig. 5a. An interface zone connects both layers. This is done to avoid the fine grid resolution that is necessary for small α everywhere along the trajectory of the AD. For small $\alpha = 0°$ respectively small lateral interspace the interpolation of the flow takes place at layer 1 and the structured meshed boundary layer of the SB. At larger interspace layer 2 is used for the interpolation. Only at the left and right border of layer 1 the cell sizes fits not with the cell size of the SB at large α. Since the AD grid is located for different α at different positions in the SB grid and does not overlap at every α the complete space the AD can allocate, the grid cells in SB cannot be just spared out. Therefore next to the two grids two so called hole geometries are defined. Every hole is connected to one grid. The hole is enveloping the SB geometry respectively the AD geometry and cuts out all the grid cells of the counterpart grid within the hole. In Fig.5b the hole for the SB is marked with a dash-dotted line the one for the AD with a dashed line. The border of the holes correspond for the solver to a chimera boundary condition, where a chimera interpolation takes place.

The hybrid grids were generated with Centaur^{TM}. For all the viscous walls the distribution of y^+ shows values < 1. In front of the slender body nose the SB grid has a fine resolution. This is done to resolve the shock, the shear layer and the flow separation properly. Although in the used flow solver a grid adaptation algorithm is available this approach was preferred to save time during the simulation and a fine mesh was required anyway for the chimera technique in the current study. Since the geometry is symmetric with respect to the pitching plane and the oncoming flow has no sideslip, only a mesh for a half-model is generated and simulated.

(a) AD grid (b) SB grid (c) Ad and SB superimposed

Figure 4: Chimera grid components.

3. Numerical Approach

The current study has been performed with the DLR TAU-code [18]. TAU is solving the steady and unsteady, three dimensional, time-accurate Reynolds averaged Navier-Stokes equation using a finite volume formulation on hybrid unstructured grids. To closure the system of equations algebraic-, one- and two equation turbulence models and Reynolds

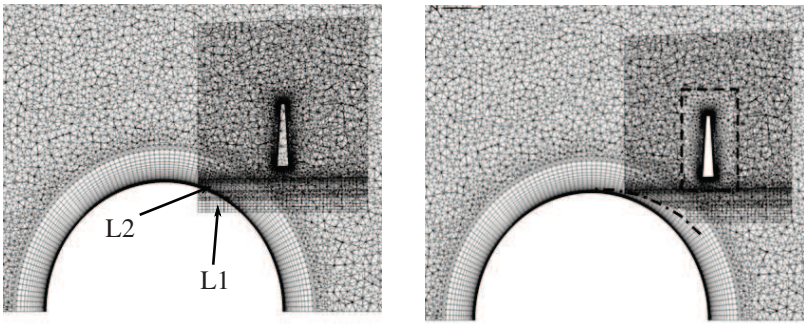

(a) W/O hole (b) With hole

Figure 5: Cutting hole chimera technique.

stress models (RSM) and explicit algebraic Reynolds stress models (EARSM) are implemented. In the current study the one equation Spalart-Allmaras turbulence model is used, like it is implemented in TAU [19]. In preliminary studies at $M = 1.41$ this turbulence model showed good results with respect to a closed separation about the interspace between the disk and the SB nose. In the experiments [16] also a closed separation was oberved for this Mach number. The same could be achieved with a Wilcox k-Ω turbulence model [20]. To save simulation time in this test study the Spalart-Allmaras turbulence model was preferred. Simulations with a SST model showed a retarded separation [2]. For flux discretization a second order AUSMDV upwind scheme is used. The disretization in time is done by an explicit Runge Kutta scheme. The viscous walls of the disk and the frame of the AD were defined as laminar while the vanes and the SB were defined as turbulent. In the experiment the disk consists of an porous material to increase the effectivness of the aerodisk [21]. For simplification this was neglected in the numerical simulations. As test case for the numerical investigation the flow conditions of the lowest tested Mach number in [16] were chosen: $M = 1.41$, $Re = 290000$. Smaller Mach numbers are more critical in order to form a closed separation like in Fig. 2b. Therefore this Mach number was chosen because if it works at this M it will work also for higher M. For all aerodynamic coefficients and the Reynolds number the missile diameter $d = 0.036\ m$ is used as reference length. The pitching motion of the SB was defined with a python script. An interface in TAU makes it possible to define via python an arbitary motion of a body. The induced flow field due to the motion is considered in the (U)RANS equation of the TAU-solver [22]. Like in the experiments the motion is a sinusoidal with a frequence of $f = 5\ Hz$ and an amplitude of 10° resulting in a range of angle of attack of $0° < \alpha < 20°$. In the wind tunnel experiment [16] the pivot point of the pitching motion was downstream of the missile rear. Even though only the forebody of the wind tunnel model is simulated the same kinematic relations (distance of the nose to the pivot) like in the experiment are applied .

In contrast to the motion of the SB the AD motion is induced due to aerodynamic forces. Therefore a 6DOF-flightmechanic tool is necessary. This tool is coupled with the flow solver (Fig.6). As input values the 6DOF-tool gets the aerodynamic forces and the inertia tensor. Considering the equation of motion the 6DOF-tool calculates the pitching rate and a new α of the AD. The 6DOF tool and the flow solver are coupled several times per pyhsical time step, see Fig.6. The exact number of coupling cycles can be defined by the user. A convergence study with respect to time provided a time step of $t = 0.0001s$. In the convergence study also the physics in the separation have been taken into account. The timestep must be small enough to ensure that the time interval to overcome the distance between separation and reattachment is discretized several times. Before each interchange of the Input data respectively the Output data a user specified amount of inner iteration is done on solver side and 6DOF side. A more detailed description of the 6DOF-tool for TAU can be fined in [22]. In general it uses the apporach of [23].

Since the numerical as well as the experimental investigations were performed at supersonic Mach numbers for this specific case at $M = 1.41$ the parts far behind the slender body forebody are not influencing the flow at the nose respectively at the AD. Therefore the numerical results of the simplified model can be compared with convenient experimental data.

4. Preliminary Investigations

The quality of the chimera grid was tested before the self-aligning-aerodisk concept was numerically investigated on a pitching slender body. Therefore a common grid (no chimera technique) was generated for the same geometry that is assembled with the chimera grid (Fig. 4c). On both grids the flow has been simulated for the defined flow condition in Chapter 3 except the Mach number was 2.2. For the test case the AD was aligned with the SB and both aligned with the oncoming flow($\alpha = 0°$). In Fig. 7 pressure isolines are shown for both simulations in the symmetry plane and in

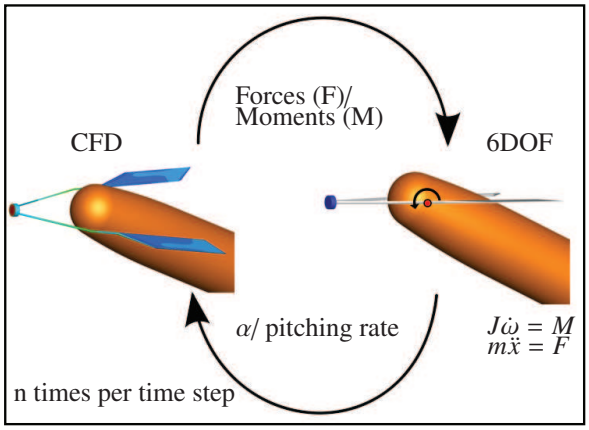

Figure 6: Coupling of CFD and 6DOF.

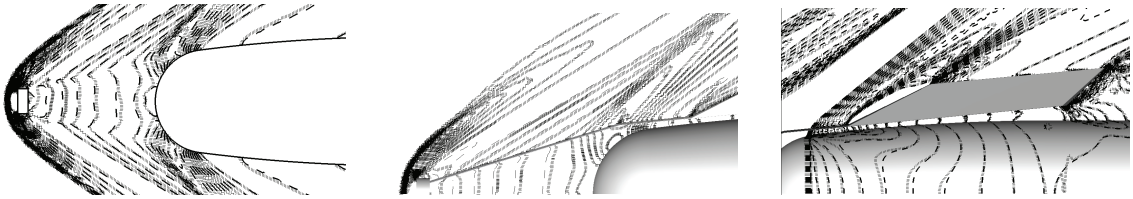

(a) Symmetry plane (b) yawing plane (c) yawing plane at vanes

Figure 7: Comparison of results of simulations with chimera technique and a standard grid (dashed line).

the plane rectangular to it (yawing plane). The dashed line corresponds to the simulation on the common grid. At the gap between the aerodisk and the nose the interpolation over the shock and within the separation does not lead to large deviations of the isolines. In front of the SB nose the isolines are more or less coincident again. At the small interspace between the wing and the SB the agreement of both solutions is even better (Fig. 7c). The investigation showed in total a good agreement between the chimera grid an the common grid. Also at locations where the physics is quite complicated the solution is not changed due to the interpolation. A reflection or refrection of the shock a the chimera boundaries is not observable.

5. Results

The simulation of the pitching slender body with a self-aligning aerodisk was not started from scratch. It was restarted from a solution of the simulation of a straight flight. The angle of attack of the SB α_{SB} and the angle of attack of the AD α_{AD} were zero. From this condition the coupling of the flow solver and the 6DOF-tool was started with a pitch-up motion of the SB.

The dependency of the solution on the number of simulated periods is shown in Fig. 8a. Fig 8a shows the misalignment of the AD with respect to the oncoming flow in dependence of α_{SB}. In total two and a half period are simulated. The wavy curve belongs to the first period of the simulation. But just for the pitch-up part this wavy behaviour is observable. For the pitch-down part the curve of the first and the second period are more or less coincident already. The same behaviour is observable for the pitch-up part of the second and the third period. After the first period the simulation can be considered as converged. A variation in time step, number of coupling cycles and inner iteration were tested for the third period too. No difference in the solution occured.

In contrast to α_{AD} the difference between the first and second period for the drag coefficient C_W is not so large (Fig.8b). It can be concluded that a small variation in α_{AD} does not result in significant changes on the drag coefficient. The drag coefficent in Fig.8b shows a trend similar to a hysteresis. This is due to the pitching motion. The pitching motion induces a velocity component v_i along the pitching body ($v_i = \omega r$). This velocity v_i is superimposed with the oncoming flow changing the oncoming flow direction locally at the SB. Because of the relation $v_i = \omega r$ at every position of the roll axis of the body a different effective angle of attack exists α_{eff}. In Fig. 9 this relation is illustrated. That means for a pitch-down maneuver that α_{eff} is larger than α and vice versa for a ptich up maneuver. A larger angle of attack results in a larger C_W. This explains the trend of C_W in 8b.

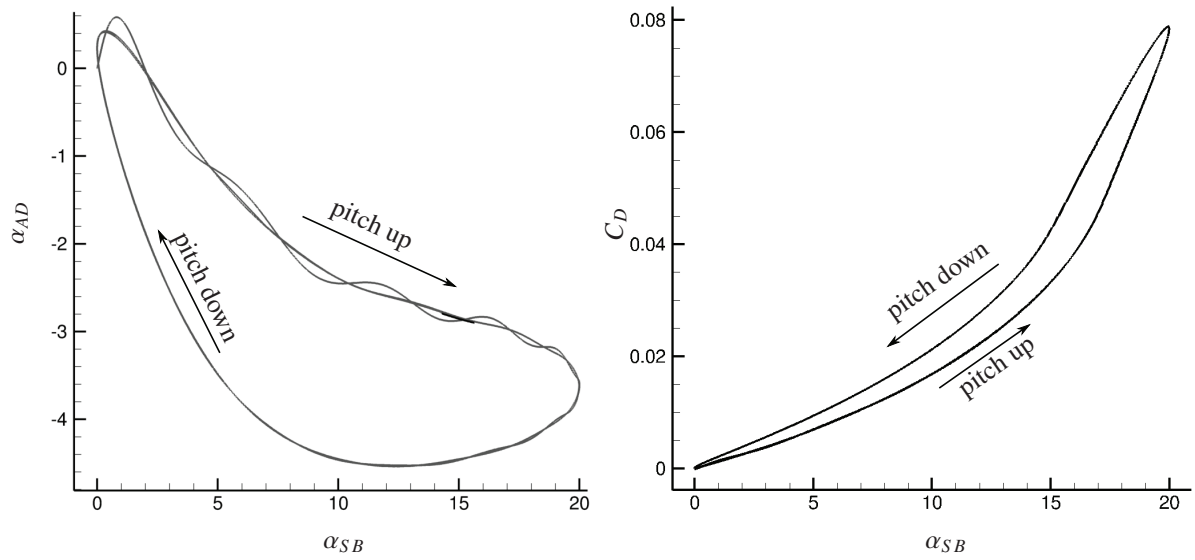

(a) α_{AD} vs. α_{SB}

(b) C_D of the model vs. α_{SB}

Figure 8: Time dependency of α_{AD} and C_w .

Fig. 8a shows that the self-aligning aerodisk concept works well. Even though a small misalignment of the AD exists at large α_{SB}. In the experiment misalignments of the same order were observed. These misalignments are due to the presence of the SB. The influence of the SB on the flow with respect to the vanes increases with increasing angle of attack. A main issue is the change in flow direction due to the SB. At the vanes at high α_{SB} the flow direction differs from the flow direction of the oncoming flow and hence the AD cannot be aligned with the oncoming flow. This effect is captured from the simulation (CFD-6DOF) and verifies its accuracy.

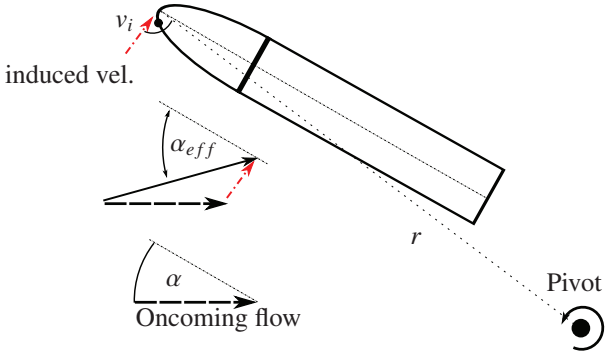

Figure 9: Sketch of the flow on a pitching SB.

In Fig. 10 a shadowgraphy of the experiment is compared with a density gradient plot at the symmetry plane of the simulation for M = 1.41 and $\alpha_{SB} = 17.7°$ (pitch-up). The agreement of both results is very good. The dominant flow features are captured from the CFD. One effect of the misalignment of AD is that the shear surface does not reattach completely on windward side, in the experiment and in the simulations (Fig. 10). The closed separation is transformed to an open separation. To analyse the impact of this effect two additional static simulations at $\alpha_{SB} = 17.7$ have been done. For one simulation (ideal case) α_{AD} was zero for the other one (real case) α_{AD} was identical with the misalignment of the AD in Fig. 10a ($\alpha_{AD} = 3.06°$). Because both are static simulations no induced velocity exists and the influence of the displaced shear surface can be analysed separately. On windward side the pressure coefficient of c_p is lower for the real case in comparison with the ideal case because of the absence of a pressure increase due to a reattachement of the shear surface (Fig. 11). Therefore significant higher c_p values exist at the reattachment of the shear surface on the upper half. In Fig. 11 a deviation of the reattachment position on the upper half at the symmetry plane between both cases is observable. This is also illustrated if Fig. 12. The reattachment of the ideal case is further

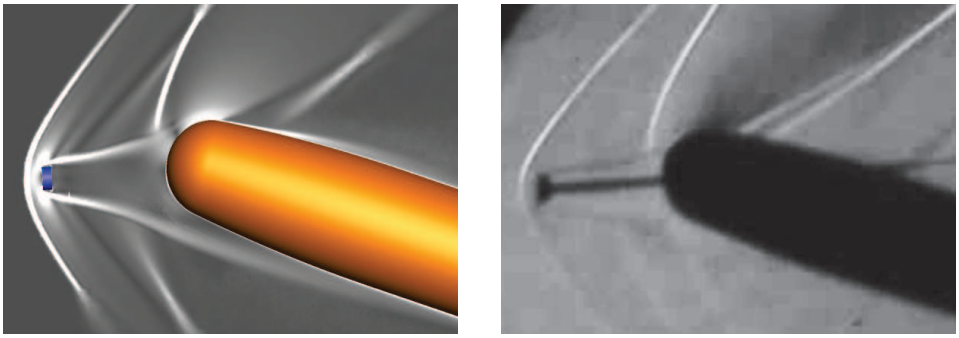

(a) symmetry plane at vanes (b) symmetry plane at vanes

Figure 10: Comparison of experimental and numerical results. Shadowgraphy and density gradients in the symmetry plane (CFD) for M = 1.41, $\alpha = 17.7°$ (pitch-up) .

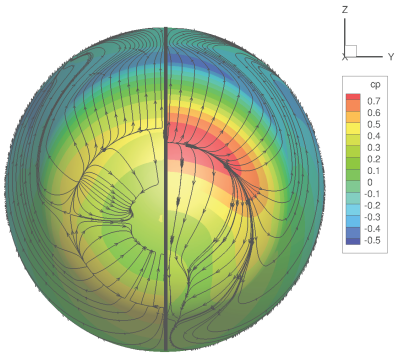

Figure 11: Effect of the misalignment on the pressure distribution at M =1.41 and $\alpha_{SB} = 17.7°$ (left side: ideal case, right side: real case).

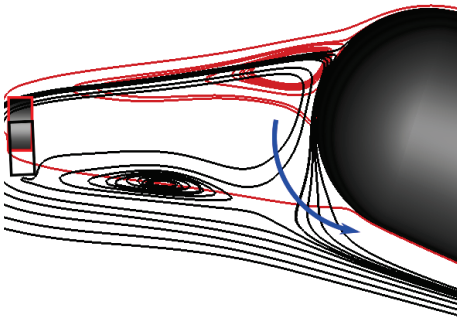

Figure 12: Streamlines in the symmetry plane (red lines: ideal case, black lines: real case).

downstream and the angle between the shearlayer and the surface is therefore smaller resulting in a smaller pressure increase at reattachment. For the real case due to of the high pressure on the upper side of the nose the mass flow within the separation is forced to stream towards the symmetry plane and downstream in direction of the blue arrow in Fig. 12. See also the surface streamlines in Fig. 11. This mass flow forms a vortex that is responsible for the displacement of the shearlayer on windward side (Fig. 13). The effect of the misalignment increases the drag of the nose about 8% for the total SB about 4%.

In Fig. 14 the drag of a pitching SB with a self-aligning aerodisk is compared with the drag of pitching SB without an aerodisk. The drag is normalized with the drag of a SB with AD at $\alpha_{SB} = 0°$ and $\alpha_{AD} = 0°$. Only one period (second) is shown. About the total range of α the drag can be reduced with a self-aligning aerodisk. The beneficial effect of an aerodisk on the wave drag of a SB is succesfully extended to high angles of attack. Although the Mach number is quite small a decrease in drag of 6.5% can be achieved at $\alpha_{SB} = 20°$. With increasing Mach number the beneficial effect of a self-aligning aerodisk should be increased even further. As expected the largest decrease in drag is at $\alpha_{SB} = 0°$ the lowest at $\alpha_{SB} = 20°$. At $\alpha_{SB} = 20°$ the decrease in drag is lower because of two reasons. One reason is the misalignment of the AD the other one is the increasing impact of the cylindrical part with increasing α on the drag.

6. Conclusion

A device to extend the effect of an aerodisk on the wave drag of a slender body to higher angle of attack was investigated numerically. The aerodisk in the current work can pitch about the slender body nose and is aligned to the oncoming flow due to aerodynamic lifting surfaces. The flow solver was coupled with a 6DOF-tool to realize the self-alignement. The device was tested on a slender body pitching sinusoidal with a frequency of 5 Hz in the range of α of $0° \leq \alpha \leq 20°$ at $M = 1.41$. For this test conditions experimental data exists to validate and compare the results of the simulations. Additionally numerical simulations of a slender body without a self-aligning aerodisk have been performed. The

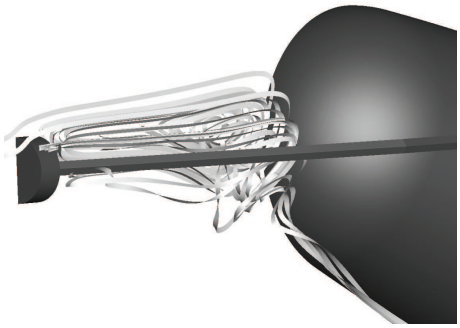

Figure 13: Visualization of the vortex on windward side.

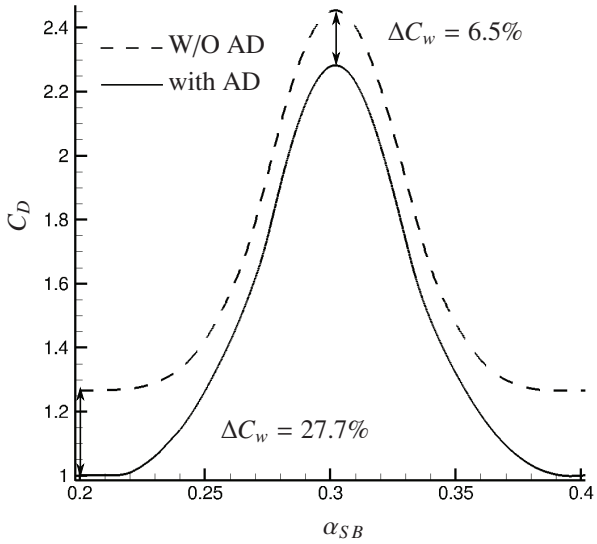

Figure 14: Influence of a self-aligned aerodisk on the drag.

numerical investigation showed that the self-aligning aerodisk is capable of decreasing even for the low test Mach number the drag about the total range of α in comparison with a slender body without this device. For higher angles of attack the influence of the self-aligning aerodisk is decreased due to a small misalignment of the aerodisk with respect to the oncoming flow. This misalignment is a result of the disturbance of the flow due to the slender body. A qualitatively comparison of the shock structure and the separation size between the experiment and the numerical investigation showed a very good agreement. A misalignment of the aerodisk is also observable in the experiment and is of the same order like in the numerical simulation. The comparison with the experiment proves the correctness of the modeling of the self-aligning aerodisk. Based on this work in a next step the complete missile configuration used in [16] will be simulated and quantitatively compared.

References

[1] Eggers, A. J., Meyer, M.,Resnikoff, D., and H. Dennis. 1956. Bodies of revolution having minimum drag at high supersonic airspeeds. NACA Technical Report. TN 3666.

[2] P. K. Chang. 1970. Separation of flow. Pergamon Press.

[3] S. R. Alexander. 1947. Results of tests to determine the effect of a conical windshield on the drag of a bluff body at supersonic speeds. NACA RM. No. L6K08a.

[4] Kim, J-H., Matsuda, A., Sakai, T. and A. Sasoh. 2011. Wave Drag Reduction with Acting Spike Induced by LASER-Pulse Energy Deposition. *AIAA Journal*. vol49.

[5] Schülein, E., Zheltovodov, A. A.,Pimonov, E. A. and M. S. Loginov. 2010. Experimental and Numerical Modeling of the Bow Shock Interaction with Pulse-Heated Air Bubbles. *International Journal of Aerospace Innovations*. Vol.2. No. 3.

[6] Schülein E. and Zheltovodov A. 2011. Effects of steady flow heating by arc discharge upstream of non-slender bodies. *Shock Waves*. Vol. 21. S.383-396. Springer Verlag, DOI: 10.1007/s00193-011-0307-1. ISSN 0938-1287.

[7] Knight, D., Kolesnichenko, Y. F., Brovkin, V. and D. Khmara. 2008. High Speed Flow Control Using Microwave Energy Deposition. *46th AIAA Aerospace Sciences Meeting and Exhibit*.

[8] Hayashi, K., Aso, S. and Y. Tani. 2005. Numerical Study of Thermal Proteciont System by Opposing Jet. *43th AIAA Aerospace Sciences Meeting and Exhibit*

[9] Meyer, B., Nelson, H. F., and D. W. Riggins.2001. Hypersonic Drag and Heat- Transfer Reduction Using a Forward-Facing Jet. *Journal of Aircraft*. vol. 38, No. 4.

[10] Fomin, V. M., Maslov, A. A., Malmuth, N. D., Fomichev, V. P., Shashkin, A. P., Korotaeva, T. A., Shiplyuk, A. N., and Pozdnyakov, G. A. 2002. Influence of a Counterflow Plasma Jet on Supersonic Blunt-Body Pressures. *AIAA Journal*. Vol. 40. No6.

[11] J. S. Shang. 2002. Plasma Injection for Hypersonic Blunt-Body Drag Reduction. AIAA Journal. Vol. 40. No.6.

[12] M.Y.M., Ahmed, and N. Qin. 2011. Recent advances in the aerothermodynamics of spiked hypersonic vehicles.*Progress in Aerospace Sciences*. Vol 47. No 6.

[13] J. R., Stalder, and H. V. Nielsen. 1954. Heat Transfer from a hemisphere-cylinder equipped with flow-separation spikes. NACA TN 3287.

[14] E. Schülein. 2008. Wave Drag Reduction Approach for Blunt Bodies at High Angles of Attack: Proof-of-Concept Experiments. *4th Flow Control Conference*. AIAA 2008-4000.

[15] E. Schülein.2010. Patent. Flying object for transonic or supersonic flight. US 7,7775,480 B2

[16] Wysocki, O., Schülein E. and C. Schnepf. 2012. Experimental Study on Wave Drag Reduction at Slender Bodies by a Self-aligning Aerospike. STAB 2012.

[17] Madrane, A, Raichle, A., and A. Stürmer. 2004. Parallel Implementation of a Dynamic Overset Unstructured Grid Approach. *Proceeding of the Third International Conference on Computational Fluid Dynamics*. ICCFD3

[18] Schwamborn, D., Gerhold, T and R. Heinrich. 2006. The DLR TAU-Code: Recent Application in Research and Industry. *European Conference on Computational Fluid Dynamics*. ECCOMAS CFD.

[19] DLR. 2012.Technical Documentation of the DLR TAU-Code. Release 2012.1.0. 2012

[20] D. C. Wilcox. 1998. Turbulence Modeling for CFD. DCW Industries. La Canada. California

[21] E. Schülein. 2010. Shock-wave control by permeable wake generators. *5th Flow Control Conference*. Illinois. AIAA2010-4977.

[22] Heinrich R., and A. Michler. 2009. Unsteady simulation of the encounter of a transport aircraft with a generic gust by CFD flight mechanics coupling. *CEAS 2009 European Air and Space Conference*

[23] Murman S. M., Aftosmis, M. J., and M. J. Berger. 2003. Simulations of 6-DOF Motion with a Cartesian Method. *41st AIAA Aerospace Sciences Meeting*. AIAA 2003-1246.